MEMS for Ultra-High Density Hard Disk Drives

D. A. Horsley[+*], S. Aggarwal[+*], R. Horowitz[+*], A. P. Pisano[+] and A. Singh[+]

[+]Berkeley Sensor and Actuator Center
[*]Computer Mechanics Laboratory
University of California at Berkeley, CA, 94720-1740

Abstract

Rotary electrostatic microactuators, suitable for use in a two-stage servo system for magnetic disk drives, have been fabricated using the HexSil process. These devices are shown to be capable of positioning the read/write elements of a 30% (pico) slider over a full ± 1 μm range, with a predicted bandwidth of 2 kHz. Continuous-time control dual-stage servos were designed and simulated using the μ synthesis technique. A Sequentially designed Single-input/single-output (SISO) and multi-input/multi-output (MIMO) control design methods have been shown to be capable of meeting prescribed uncertainty and performance specifications.

1   Introduction

The areal density of magnetic disk-drives is increasing at an annual rate of 60% and is expected to reach 10 GBit/in^2 by the turn of the century [5]. Until recently, these increases have been achieved by a combination of increased track pitch - which is the number of tracks per inch along the radius of the disk - and an increase in linear bit density - which is the number of bits written along one inch of a track. Increases in bit density require either more sensitive head elements or reduced flying height. Tribological problems posed by contact and near-contact recording have been delayed by the introduction of Magneto-Resistive (MR) heads, which allow higher flying heights due to their greater sensitivity compared to inductive elements. However, given that current bit densities are approximately ten times greater than track densities, significant areal density increases can be achieved by reducing the track width without reducing flying height or resorting to Giant Magneto-Resitive (GMR) heads.

To achieve the goal of 10 GBit/in^2, linear track densities must exceed 25,000 tracks-per-inch, resulting in tracks which are 1 μm wide and an allowable servo tracking accuracy of 100 nm. Because conventional servo actuators cannot provide this level of tracking accuracy, the use of a microactuator for high-bandwidth, high accuracy positioning has been proposed. To date, these designs have been of three distinct types. The first type may be classified as an actuated suspension. In this approach, conventional assembly and machining techniques are used to integrate an electromagnetic or piezoelectric actuator into a conventional steel suspension [12, 9]. A disadvantage to these designs is that they locate the actuator far from the read/write elements and therefore have a limited bandwidth due to suspension vibration. The second type may be classified as an actuated head, in which the actuator is located on the slider and the read/write elements are placed on top of the actuator [3, 10, 7]. The critical limitation of this approach is that the actuator fabrication process must be compatible with the head/slider fabrication process. The actuators discussed in this paper are of the third type, where the actuator is placed between the slider and the gimbal of a conventional suspension [4, 6].
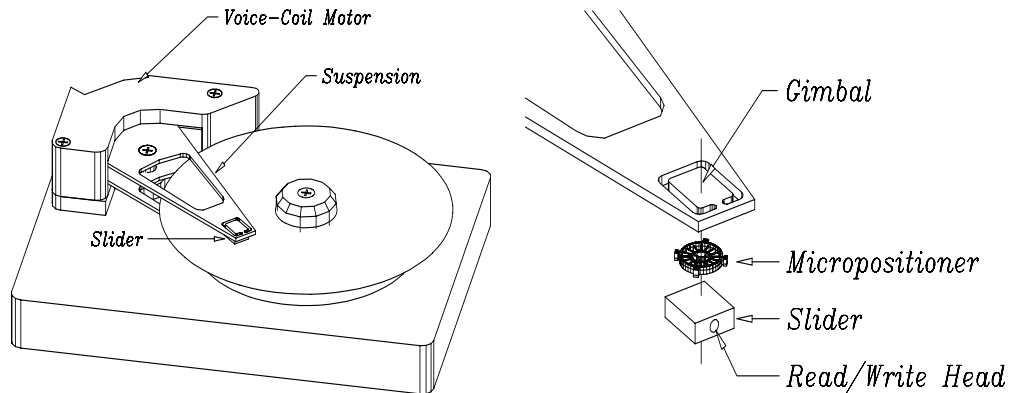
2   Microactuator Design and Fabrication

Figure 1: Left - Servo positioning mechanism of a conventional magnetic disk-drive. Right - Exploded view of the microactuator assembly. The microactuator is sandwiched between the slider and a conventional gimbal.

Fig. 1 shows the servo-positioning mechanism of a conventional disk-drive. Read and write elements which transfer data to and from the disk are embedded in a ceramic slider which is bonded to a gimbal at the end of the stainless steel suspension. An electromagnetic voice-coil motor (VCM) attached to the opposite end of the suspension is used to move the slider radially across the disk. The controlled variable is the position error signal (PES), which is the measure of the deviation of the read/write element from track center.

The conventionally actuated servo bandwidth is limited by mechanical resonances in the suspension. Increased tracking accuracy can be provided by a dual-stage control system, using the VCM for coarse positioning, and a microactuator mounted between the slider and suspension for fine positioning [6, 1]. A close-up of the slider/microactuator assembly is shown in Fig. 1. An angular actuation scheme was selected for the microactuator because it allows high lateral stiffness, minimizing the sensitivity of the device to shock loading in the plane of the disk. A rotation of 2 mrad produces a linear translation of 1 μm at the read/write head. As shown in Fig. 2, the actuator consists of a fixed outer ring, or stator, and a mobile
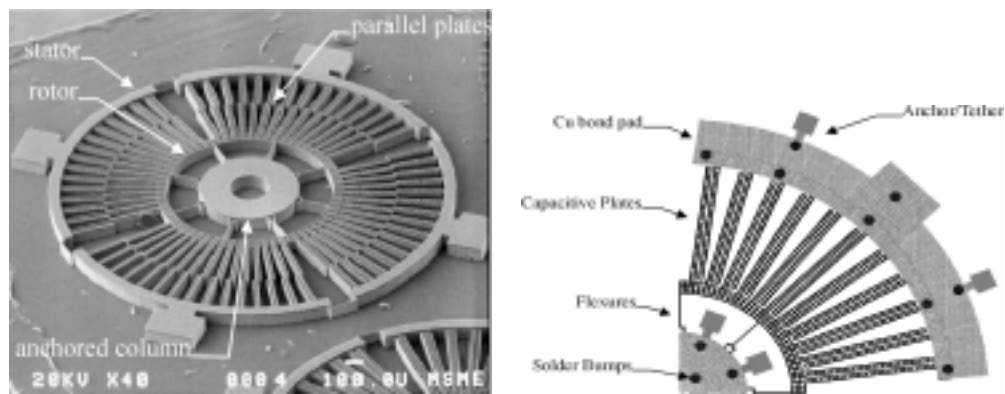

Figure 2: Left - SEM of 100 μm high, 2.6 mm diameter structure. Right - One quarter of the quad-symmetric actuator layout.

inner ring, or rotor, which is connected to an anchored central column via narrow polysilicon

flexures. Actuation is accomplished via parallel plates which are attached to the rotor and stator in opposing pairs. A voltage applied across these plates results in an electrostatic force which rotates the central rotor. The stator is made up of four separate, electrically isolated quadrants. In Fig. 2 the isolation is achieved with thin break-away beams connecting the stator quadrants. An electrostatic design was chosen for ease of fabrication. The structural material of the device need only be conductive, rather than ferromagnetic or piezoelectric. Furthermore, electrostatic actuators allow high accuracy capacitive measurement of displacement and are capable of high-bandwidth operation [3].

2.1 Fabrication Method

The height to width aspect ratio of an electrostatic actuator is an extremely important design parameter for two reasons. Firstly, for a fixed capacitive gap, the actuator torque output is linearly proportional to the structural height, and therefore increases linearly with aspect ratio. Secondly, it is important that any uncontrollable, cross-axis resonances be well above the servo bandwidth. For flexures with rectangular cross section, the ratio of the cross-axis modes to the in-plane modes increases linearly with aspect ratio. Until recently, methods for producing high aspect-ratio structures relied on long etches in plasma chambers which can accommodate only one wafer at a time. The HexSil process allows the fabrication of high aspect-ratio, molded CVD polysilicon structures [8]. The unique feature of this process is that it relies on a re-usable silicon mold, significantly lowering the price of finished parts. After fabrication, the finished structure is solder bonded to a target substrate and the mold wafer is ready for the next fabrication cycle. One quarter of the quad-symmetric microactuator layout is shown in Fig. 2. The structural material is in-situ phosphorous doped polysilicon, which is metallized with copper on the bonding surfaces to create solder-wettable pads. The solder bumps shown in Fig. 2 are plated on a target die and optically aligned to these pads during the transfer process [11]. Thin polysilicon tethers are used to anchor the structure to the mold wafer before bonding. A simplified fabrication process flow is shown in Fig. 3.
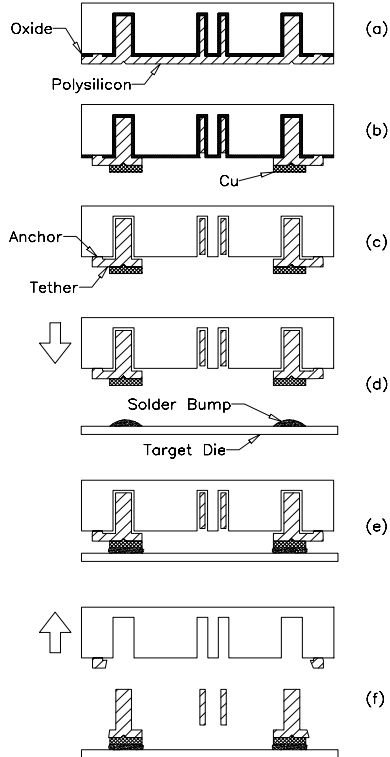
Fig. 3: Fabrication Process Flow

The first step is to use reactive ion etching (RIE) to etch deep trenches into a silicon mold wafer. The depth of the trenches determines the height of the fabricated structure. Next, a two level sacrificial oxide layer is deposited. The first layer consists of 1 μm of phosphosilicate glass (PSG) which is used to provide a fast-etching release layer. However, a second layer of 3 μm of conformal SiO_2 is needed to coat the trench sidewalls. Anchor holes are patterned through the oxide, after which the structural layer of doped polysilicon is deposited by CVD (a). This polysilicon makes contact with the silicon mold wafer at the anchor points. The surface polysilicon is then patterned, leaving pads for mounting the actuator. A plating seed layer consisting of a 50 $\overset{\circ}{A}$ Cr adhesion layer beneath 1000 $\overset{\circ}{A}$ Cu is evaporated onto the wafer surface. Next, copper bonding pads are electroplated using a 4-5 μm thick photoresist mask as a plating mold (b). After electroplating, the photoresist is stripped in acetone, and the thin seed layer is removed from the unplated areas by ion-milling. The sacrificial oxide is removed by an etch in concentrated hydrofluoric acid, which etches the PSG layer at approximately 20 μm/min, but does not significantly attack the copper for etch times of up to 60 minutes.

After the oxide etch, the structure is held in the mold by thin polysilicon tethers which will break away when the structure is transferred to a target die (c). The copper mounting pads on the actuator are optically aligned to solder bumps on the target (d), and the two dice are contacted together (e) for solder reflow. After the bond has cooled, the two dice are separated, breaking the thin tethers and leaving the released actuator bonded to the target substrate (f). Residual polysilicon from the break-away tethers may be removed from the mold wafer with a long HF etch or by mechanical polishing.

2.2   Fabrication Results

Two succesful fabrication runs were made, the first using mold wafers which were etched to a depth of 100 μm using a deep silicon etcher manufactured by ST Systems. The actuators fabricated in this first run were used to develop the solder-bump transfer process. Unfortunately, the mold wafers were destroyed before the process was fully developed, so these structures were not actuated. The second fabrication run used wafers which were only etched to a depth of 30 μm due to equipment limitations.

A 100 μm high structure from the first run which was released and transferred onto an adhesive pad is shown in the left hand side of Fig. 4. The 3.25 μm wide flexures connecting the rotor to the anchored central column were fabricated with a maximum aspect ratio of 30:1, while the 14.75 μm capaci- tive gap had a maximum aspect ratio of 7:1. The aspect ratio of HexSil beams can be much greater than that of the gaps between them, since the beam spacing is determined by the separation of the mold trenches plus twice the thickness of the sacrificial oxide layer. In turn, the minimum separation between the mold trenches is determined by the aspect ratio of the RIE process used to create the mold. The maximum available RIE aspect ratio is currently 25:1, yielding a maximum capacitive gap aspect ratio of approximately 12:1. The beam thickness, on the other hand, may be as thin as 1-2 μm, so aspect ratios of 100:1 are possible. Note that in both actuator designs, the rotor and
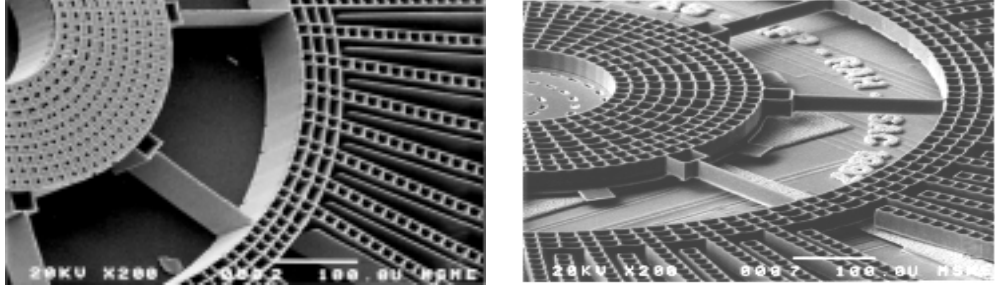
4

Figure 4: Left - SEM showing 100 μm high flexures connecting the rotor to the anchored central column. Right - SEM of an actuator which has been solder bonded to a target die. Several broken tethers are visible around the left portion of the central hub.

stator elements are not mechanically connected, and must be transferred with high accuracy to maintain a balanced actuation force. The right hand side of Fig. 4 shows a 30 μm high actuator which has been solder bonded to a target die. The rotor and capacitive plates are suspended approximately 8 μm above the target substrate, leaving them free to rotate. Also visible are the mold tethers which were broken after solder bonding the structure to the target.

3 Actuation Dynamics

The microactuator rotor is coupled to the fixed stator via mechanical flexures, and the dynamics of the device can be expressed as a second-order system:

$$J_t\ddot{\theta} + c\dot{\theta} + K_\theta\theta = \tau(v_1, v_2, \theta),\tag{1}$$

where J_t is the combined moment of inertia of the slider and microactuator rotor, c is the damping, K_θ is the mechanical spring stiffness of the flexures, and $\tau(v_1, v_2, \theta)$ is the electrostatic torque.

Electrostatic torque is produced by $2N$ capacitive plate pairs, half of which rotate the microactuator clockwise, the other half counter-clockwise. For small rotation angles, θ, these plates may be modeled as parallel plate capacitors separated by gaps x_1 and x_2 defined by

$$x_1 = x_n - r\theta \quad x_2 = x_n + r\theta,\tag{2}$$

where r is defined to be the distance from the centroid of the plate to the center of rotation of the rotor and x_n is the nominal capacitive gap with zero rotation. Applying a voltage v_1 to one half the structure and v_2 to the other half, and substituting the values for x_1 and x_2 given in Eq. (2) yields

$$\tau(v_1, v_2, \theta) = \frac{1}{2}Nr\epsilon_o A\left[\left(\frac{v_1}{x_n - r\theta}\right)^2 - \left(\frac{v_2}{x_n + r\theta}\right)^2\right],\tag{3}$$

where A is the area of each plate and ϵ_o is the permittivity of air.

A common method for linearizing the quadratic voltage nonlinearity of the electrostatic force is to use a differential driving scheme with a fixed bias voltage, v_b, and a variable control voltage, v_c [4].

$$v_1 = v_b + v_c, \quad v_2 = v_b - v_c\tag{4}$$

Assuming small rotations about $\theta = 0$, the electrostatic torque may then be approximated by

$$\tau(v_1, v_2, \theta) = \tau(v_c, \theta) = k_v v_c + k_e\theta,\tag{5}$$

5

where k_v represents the gain from voltage to torque and k_e is the so-called *electrostatic spring constant*. k_v and k_e are respectively given by

$$k_v = \frac{\partial}{\partial v_c} \tau(v_c, \theta)|_{(0,0)} = \frac{2Nr\epsilon_o Av_b}{x_n^2}, \quad k_e = \frac{\partial}{\partial \theta} \tau(v_c, \theta)|_{(0,0)} = \frac{2Nr^2\epsilon_o Av_b^2}{x_n^3}. \quad (6)$$

3.1 Linearized Model

Substitution of Eq. (5) into Eq. (1) yields a linear dynamic model.

$$J_t \ddot{\theta} + c\dot{\theta} + (K_\theta - k_e)\theta = k_v v_c \quad (7)$$

The linearized system is stable for $K_\theta > k_e$, implying that the non-linear system given by Eq. (1) is stable for small rotations. Note that the effect of the electrostatic spring term, k_e, is to de-stabilize the system, reflecting the tendency of the capacitive plates to pull-in for sufficiently high voltage. The maximum bias voltage for which the microactuator remains stable is found by setting the electrical spring stiffness in Eq. (6) equal to the mechanical spring stiffness and solving for v_b, which yields

$$v_{b,max} = \sqrt{\frac{x_n^3 K_\theta}{2Nr^2\epsilon_o A}}. \quad (8)$$

Note that values of $v_b > v_{b,max}$ will result in instability with zero rotation. Experimental measurements of the static rotation characteristic of the actuator were performed by applying differential drive voltages with $v_b = 38$ VDC and $-38V < v_c < +38V$ to the two halves of the stator. The experimental data was fit with a theoretical model corresponding to the steady-state solution to Eq. (1). Because both the flexural stiffness, K_θ, and the capacitive gap, x_n, depend on the polysilicon beam width, the fit was achieved by adjusting this width in the model, until it matched the value given by the steady-state solution to Eq. (1). Using these experimental results, the values for k_e, k_v, and K_θ were extracted from the model.

The resonant frequency of the linearized system from Eq. (7) is given by

$$f_n(v_b) = \frac{1}{2\pi}\sqrt{\frac{K_\theta - k_e(v_b)}{J}}. \quad (9)$$

Note that k_e, the electrostatic spring constant, is a function of the bias voltage.

	units	design 1	design 2
# Plates, N	–	22	30
K_θ	$\mu\frac{\text{N m}}{\text{rad}}$	29	29
k_v	$\frac{\mu\text{N m}}{\text{V}}$	1.1e-3	1.5e-3
k_e	$\frac{\mu\text{N m}}{\text{rad}}$	2.6	3.6
τ_{max}	nN m	43	60
$J_{slider} + J_{rotor}$	mg m^2	3.73e-7	3.77e-7
J_{rotor}	mg m^2	6.8e-9	1.08e-8
max. BW	kHz	1.9	2.0
A_{DC}	$\frac{\mu\text{rad}}{\text{V}}$	43	60
f_n	kHz	1.3	1.3
$f_n(unloaded)$	kHz	9.9	7.7

Table 1: Actuator Design Specifications

The result of this effect is that the resonant frequency of the device may be tuned by varying the bias voltage. The left hand side of Fig. 5 shows a plot of the resonant frequency of two different microactuator designs for varying bias voltages. In this experiment, the push-pull segments of the stator were biased at $+38V$ and ground, respectively, while the rotor bias, v_b, was varied. By using the values of k_e, k_v, and k_θ extracted from the DC rotation test discussed above, the results of this experiment were used to calculate the rotor moment of inertia, J_{rotor}. The measured values are summarized in Table 1.

Using the measured parameters in Table 1, the microactuator frequency response was simulated. The right hand side of Fig. 5 shows that at high frequencies the response intersects the dotted line defined by
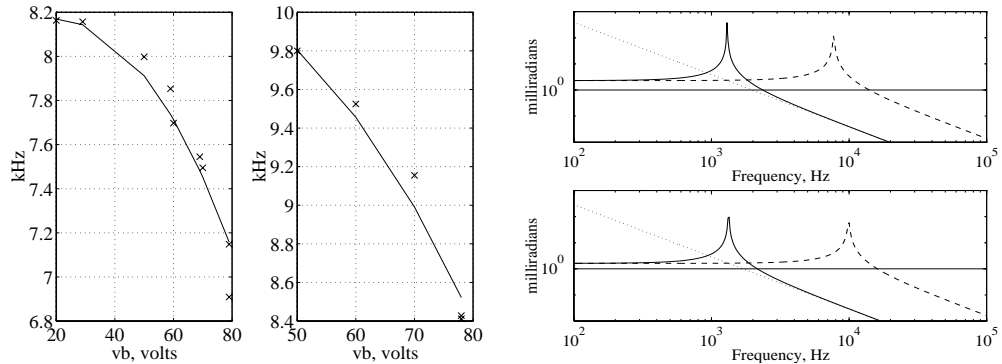
$$H(s) = \frac{k_v}{J_t s^2}. \quad (10)$$

Figure 5: Left - Actuator resonant frequencies for varying bias voltages. Right - Simulated microactuator frequency response. In each plot, the dashed line indicates the microactuator response without a slider payload, while the solid line shows the predicted response when the slider is bonded onto the microactuator rotor. The dotted line indicates the high frequency limit imposed by Eq. (10) .

This line represents a hard limit on microactuator performance, since J_t is determined by the payload, and k_v is constrained by the capacitive gap and area of the actuator. At low frequencies, the response is equal to the DC gain of Eq. (1) given by

$$\theta(v_c) = \frac{k_v}{(K_\theta - k_e)} v_c \, . \tag{11}$$

The intersection of these two lines determines the resonant frequency of the actuator. In order to allow the microactuator to be controlled, this frequency must be either well below or well above the intended closed-loop control bandwidth. To achieve a tracking accuracy of less than 100nm, it is predicted that a bandwidth of 2 kHz will be required [4]. Thus, the resonant frequency must be either below 2 kHz, or above approximately 10 kHz. However, a high resonant frequency requires lower DC gain, as shown in the right hand side of Fig. 5. Choosing a resonant frequency below 2 kHz maximizes the DC gain and allows the actuators to provide a $\pm 1 \mu$m range over the entire servo bandwidth.

4   Dual-Stage Servo Design

A dual-stage track-following servo system requires a more sophisticated controller than that of a conventional single-stage servo system. At low frequencies, where the magnitude of the track runout tends to be large, tracking must be done primarily by the arm's Voice Coil Motor (VCM), with the micro-actuator performing some fine-positioning to compensate for frictional disturbances and windage, which limit the low frequency positioning accuracy of the arm. At higher frequencies, where the magnitude of the track runout is smaller and structural resonances limit the capabilities of the arm, most of the tracking should be performed by the micro-actuator.

Two continuous-time control synthesis approaches, both based on the μ-synthesis technique [2], were investigated. The first is a two-step single-input/single-output (SISO) approach and exploits the fact that the dynamics of the arm and micro-actuator are sufficiently decoupled, since the micro-actuator inertia and force output are over 100 times smaller than those of the VCM and arm. In this approach two SISO compensators are sequentially designed. The first compensator, which has as its input the position of the micro-actuator

relative to the arm and generates a control signal for the VCM, is designed as if it was to be used in a conventional single stage servo system. The second compensator, which has as its input the PES of the head relative to the track and generates a control signal for the microactuator, is designed accounting for the fact that the first compensator is acting on the VCM, and stabilizes the overall closed loop dynamics. This design approach is also referred to as the *master-slave approach*, since VCM compensator attempts to make the arm follow the microactuator, while the microactuator compensator attempts to minimize the PES. The second approach is a multi-input/multi-output (MIMO) design, which takes full account of the coupling between the arm and micro-actuator. Block diagrams for both approaches are shown in Figure 6.
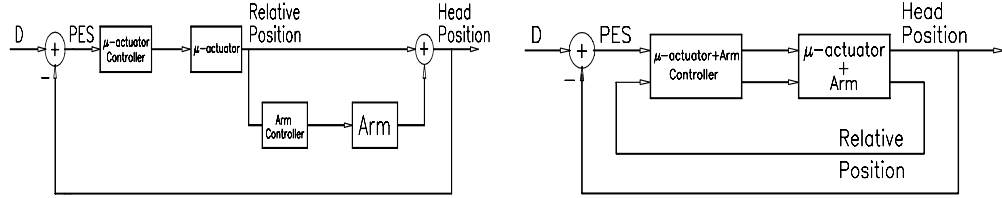

Figure 6: Left - Two-step SISO controller block diagram. Right - MIMO controller block diagram.

The dual-stage disk drive model used for the controller design and simulation is shown in the left hand side of Fig. 7. Here a linear displacement model is shown for simplicity. This simple system attempts to model the rigid body mode of the positioning system, the most significant resonance mode of the arm's suspension, which is generally the first torsional mode, and dynamics of the microactuator's suspension. The parameters used in the system model were chosen mostly based on data

obtained from commercial drives and the microactuator experiments described in the previous section. The torsional resonance of suspension was assumed to be at 2.0kHz and to have a damping ratio of 0.01. For the micro-actuator, the resonance due to the combination of the mechanical and electrical spring stiffnesses was placed at 1.0kHz, and the damping ratio was chosen as 0.5. The damping is due to drag forces which act on the slider as it flies over the disk surface on an air bearing. Unfortunately, to date no one has studied or measured the rotational or lateral dynamics of the slider relative to the suspension. To roughly model the effect of bearing stiction, the input to the arm was passed through a second order high pass filter with a cutoff of 60Hz. In this way the control input to the arm is attenuated below 60Hz, which is the approximate threshold of bearing friction effects on many drives.

Matlab's μ-synthesis toolbox [2] was used to design the compensators for the dual-stage servo systems. The block diagram used for the design is shown in the right hand side of Fig. 7. The figure shows the weighting blocks that were used to define the performance and robustness specifications. Although only the MIMO model is shown, the same weightings were used for the sequential SISO design. As shown in Fig. 7, a fictitious primed track runout input D of unity infinity-norm is scaled by a frequency dependent weight WD to generate the actual track runout D. The actual PES signal and the microactuator's relative position are respectively weighted by static gains WE_1, and WE_2 to generate the test outputs $E1$ and $E2$. The design approach is based on the fact that the μ-synthesis design algorithm of the toolbox attempts to converge, through an iterative process, to a feedback system which has a closed loop infinity-norm from D' to the test outputs. To achieve meaningful control systems designs, the weightings WD $E1$ and $E2$ must be selected so that the spectrum of model's runout D approximates that of an actual disk non-repeatable runout and the infinity-norms of both the PES and microactuator's relative position signal are within allowable values when the test outputs $E1$ and $E2$ have unity infinity-norms. To achieve robust performance and limit

the bandwidth of the control system within realistic bounds, modeling uncertainty weightings were incorporated in the block diagram. As shown in Fig. 7, the uncertainty weights WU_1 and WU_2 respectively act on the arm torque (τ_{ARM}) and micro-actuator torque (τ_{ACT}) to produce a control input uncertainty. These input uncertainties are respectively scaled by the gains d_1 and d_2. The net effect is to produce a frequency dependent percentage uncertainty on the control input. Readers are referred to [1] for further details on the design methodology and weightings selection.
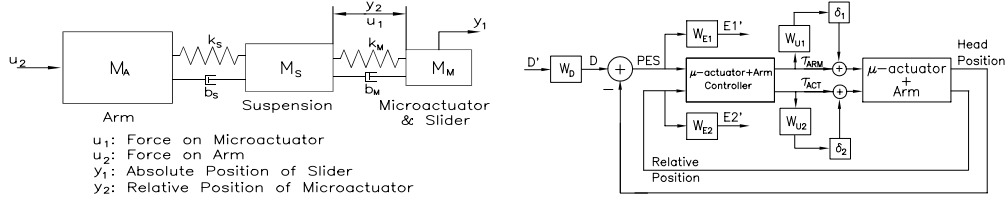

Figure 7: Left - Control system model. Right - Structured disturbance and uncertainty models.

4.1   Control Design Results

The closed-loop PES sensitivity transfer functions for both the sequential SISO and MIMO dual-stage servo designs are shown in Fig. 8. The PES sensitivity transfer function of the single-stage servo, designed for the arm alone in the first stage of the sequential SISO approach, is also shown in Fig. 8. This plot is shown in order to compare the dual-stage results with a single-stage servo system. The closed loop transfer functions from the track runout to the microactuator relative position for both dual-stage servo designs are shown in the right hand side of Fig. 8. A key feature of the PES transfer functions is that, while the single-stage
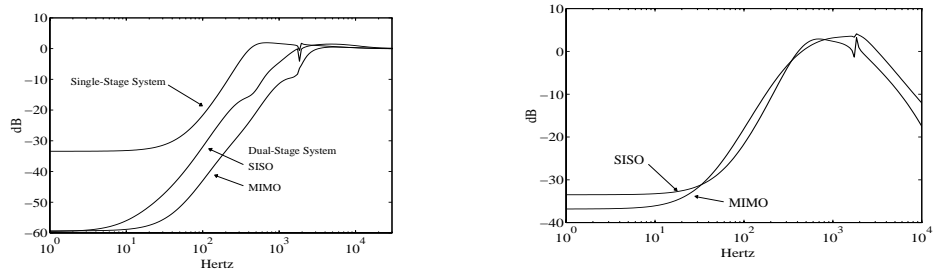

Figure 8: Left - Closed-loop PES sensitivity transfer functions for SISO and MIMO designs. Right - Runout to micro-actuator relative position transfer function for SISO and MIMO designs.

design flattens out at 60 Hz due to bearing friction, the micro-actuator enables the dual-stage designs to continue increasing the attenuation beyond 60Hz, resulting in an increased low frequency attenuation of 25dB relative to the single-stage design. The single-stage controller

achieves a low frequency PES disturbance attenuation of 33 dB with a 6 state controller and a bandwidth of 400 Hz. Both the MIMO and SISO controllers have a low frequency PES disturbance attenuation of 59 dB. The MIMO controller uses only a 9 state controller and achieves a bandwidth of 3.0 kHz. The SISO design, on the other hand, requires a 13 state controller (6 for the arm and 7 for the micro-actuator), and achieves a bandwidth of 2.0kHz. For each of the controllers, order reduction was performed by eliminating some of the states with the smallest Hankel singular values [2]. The control order for the both the MIMO and SISO designs was the minimum achievable while still maintaining robust performance. This was tested by checking that the μ value of the closed loop system was still less than unity for the reduced order controllers. As an additional measure of robustness for each of the designs, the phase and gain margins for each controller was determined. The open loop phase margin for the single-stage design is 52°, with a gain margin of 23 dB. For the MIMO and SISO designs, the margins were determined by breaking the feedback from the head position and then looking at the open loop transfer function from PES to head position. For the MIMO design, a phase margin of 60° is achieved with a gain margin of 60dB. The corresponding SISO margins are 65° and 24dB. The micro-actuator track runout tracking is very similar in both the SISO and MIMO designs. For both the SISO and MIMO designs, the relative position transfer function is near 0 dB from 400 Hz to the system bandwidths of 2.0 kHz and 3.0 kHz, respectively. This region represents the frequencies over which tracking is done primarily by the micro-actuator since in this frequency region the relative position is approximately equal to the track runout.

5   Conclusion

An angular microactuator was designed and fabricated using the HexSil process. The actuators have been shown to have a maximum range of ± 3 mrad, corresponding to a linear translation of ± 1.8 μm at the read/write magnetic heads of a 30% slider. A theoretical model for the actuator dynamics has been derived. The predicted open-loop frequency response of this microactuator will guarantee an operating range of ± 1 μm up to a frequency of 2 kHz. The finished structures were transferred from the re-usable mold wafer to a target die using a solder bond. Continuous-time dual-stage servos have been designed using the μ synthesis technique. Sequential SISO and MIMO designs have been shown to be capable of meeting the prescribed uncertainty and performance specifications. The MIMO design achieved a simulated low frequency disturbance rejection of 59 dB and a bandwidth of 3.0 kHZ

6   Acknowledgements

References

[1] S. Aggarwal, D. Horsley, R. Horowitz, and A. Pisano. Microactuators for high density disk drives. In *Proceedings of the American Control Conference*, 1997. Albaquerque, New Mexico, USA.

[2] G. Balas, J. Doyle, K. Glover, A. Packard, and R. Smith. μ-analysis and synthesis toolbox, 1995. MUSYN and Mathworks Inc.

[3] P. Cheung, R. Horowitz, and R. T. Howe. Design, fabrication, position sensing, and control of an electrostatically-driven polysilicon microactuator. *IEEE Transactions on Magnetics*, 32(1):122–128, 1996.

[4] L.-S. Fan, H. Ottesen, T. Reiley, and R. Wood. Magnetic recording-head positioning at very high track densities using a microactuator-based, two-stage servo system. *IEEE Transactions on Industrial Electronics*, 42:222–233, June 1995.

[5] Grochowski and R. Hoyt. Future trends in hard disk drives. *IEEE Transactions on Magnetics*, 32(1):1850–1854, May 1996.

[6] D. Horsley, A. Singh, A. Pisano, and R. Horowitz. Angular micropositioner for disk drives. In *10th IEEE International Workshop on Micro Electro Mechanical Systems (MEMS-97)*, January 1997. To appear in *IEEE/ASME Journal of Micro-Electro-Mechanical Systems*.

[7] T. Imamura, T. Koshikawa, and M. Katayama. Transverse mode electrostatic microactuator for mems-based hdd slider. In *IEEE Proc. 9th Int. Workshop on MEMS*, pages 216–221, February 1996.

[8] C. Keller and M. Ferrari. Milli-scale polysilicon structures. In *Solid-State Sensor and Actuator Workshop, Hilton Head*, pages 132–137, June 1994.

[9] S. Koganezawa, K. Takaishi, Y. Mizoshita, Y. Uematsu, and T. Yamada. Development of an integrated piggyback milli-actuator for high density magnetic recording. In *Intl. Conference on Micromechatronics for Information and Precision Equipment*, Paper # MR-08, July 1997.

[10] S. Nakamura, K. Suzuki, M. Ataka, and H. Fujita. An electrostatic micro actuator for a magnetic head tracking system of hard disk drives. In *International Conference on Solid-State Sensors and Actuators (Transducers '97)*, pages 1081–1084, June 1997.

[11] A. Singh, D. A. Horsley, M. B. Cohn, A. P. Pisano, and R. T. Howe. Batch transfer of microstructures using flip-chip solder bump bonding. In *International Conference on Solid-State Sensors and Actuators (Transducers '97)*, June 1997.

[12] K. Takaishi, T. Imamura, Y. Mizoshita, S. Hasegawa, and et al. Microactuator control for disk drive. *IEEE Transactions on Magnetics*, 32(1):1863–1866, May 1996.